CHEMISTRY

Direct measurements of DOCO isomers in the kinetics of OD + CO

Thinh Q. Bui,[1]* Bryce J. Bjork,[1†] P. Bryan Changala,[1] Thanh L. Nguyen,[2] John F. Stanton,[2] Mitchio Okumura,[3] Jun Ye[1]*

Quantitative and mechanistically detailed kinetics of the reaction of hydroxyl radical (OH) with carbon monoxide (CO) have been a longstanding goal of contemporary chemical kinetics. This fundamental prototype reaction plays an important role in atmospheric and combustion chemistry, motivating studies for accurate determination of the reaction rate coefficient and its pressure and temperature dependence at thermal reaction conditions. This intricate dependence can be traced directly to details of the underlying dynamics (formation, isomerization, and dissociation) involving the reactive intermediates *cis*- and *trans*-HOCO, which can only be observed transiently. Using time-resolved frequency comb spectroscopy, comprehensive mechanistic elucidation of the kinetics of the isotopic analog deuteroxyl radical (OD) with CO has been realized. By monitoring the concentrations of reactants, intermediates, and products in real time, the branching and isomerization kinetics and absolute yields of all species in the OD + CO reaction are quantified as a function of pressure and collision partner.

INTRODUCTION

Fundamental understanding and control of bimolecular reactions have long been the primary motivations for the fields of chemical kinetics and dynamics. One approach has been to construct a detailed dynamical understanding from the bottom up, exemplified by the field of crossed molecular beam experiments, where reaction dynamics are dissected from single collision processes (*1*). For applications in combustion, atmospheric, and fundamental chemistry, a broader goal from these studies is the prediction of the rates and outcomes of reactions. This knowledge requires direct connection of reaction dynamics to molecular structure and detailed understanding on how the dynamics change during the chemical transformation from reactants to products. However, transitions from reactants to products in bimolecular reactions are often multistep because of the involvement of multiple reactive intermediates, transition states, and final product channels on a multidimensional potential energy surface (PES). These factors have limited experimental characterization of the underlying dynamics, and theoretical models are often required to assist with detailed mechanistic interpretation (*2*–*4*). It is thus of particular interest to develop new experimental approaches for the study of reaction kinetics and dynamics from real-time observation of individual elementary chemical reactions.

The reaction of hydroxyl (OH) with carbon monoxide (CO), Eq. 1, exemplifies such a system that has an intricate reaction mechanism governed by multiple bound states, both reactive and nonreactive

$$\mathrm{OH + CO \xrightarrow{k_1} products} \quad (1)$$

The gas-phase kinetics of OH + CO has received considerable attention from both experimental and theoretical efforts due to its fundamental and practical importance in atmospheric and combustion chemistry (*5*). The observed rate coefficient, k_1, displays strong pressure and non-Arrhenius temperature dependence, which is now understood to arise from the formation of the HOCO complex, with subsequent tunneling to the products H + CO_2. Figure 1 shows the PES for the OH + CO reaction.

Over the past four decades, the HOCO formation mechanism had been derived from fits of the observed $k_1(P,T)$ to theoretical models (*6*–*17*). These studies led to the following proposed reaction mechanism for OH + CO, starting from the calculated asymptotic (stationary) states in Fig. 1

$$\mathrm{OH + CO \rightleftarrows HOCO^* \rightarrow H + CO_2} \quad (2)$$

$$\mathrm{HOCO^* \overset{[M]}{\rightleftharpoons} HOCO} \quad (3)$$

$$\mathit{trans}\text{-HOCO} \overset{[M]}{\rightleftharpoons} \mathit{cis}\text{-HOCO} \quad (4)$$

$$\mathit{cis}\text{-HOCO} \rightarrow \mathrm{H + CO_2} \quad (5)$$

Reaction 1 initially produces energized HOCO*, which either backreacts to OH + CO or proceeds to form H + CO_2 (Eq. 2). In the presence of a buffer gas, M, HOCO* may be collisionally stabilized (Eq. 3). At low pressures, the overall reaction rate can be represented by an effective bimolecular rate coefficient, $k_1([M],T) = k_{1a}([M],T) + k_{1b}([M],T)$, where k_{1a} and k_{1b} describe the formation of stabilized HOCO and H + CO_2, respectively.

HOCO exists as two geometrical isomers, *trans*-HOCO and *cis*-HOCO, with the latter being slightly less stable by 5 to 7 kJ mol^{-1} (*18*, *19*). Current theory predicts that both isomers will be formed by stabilization upon associative recombination of OH + CO, with the *trans*-HOCO isomer favored. Calculations indicate that the barrier for isomerization (TS4; Fig. 1) is low, leading to rapid isomerization between the two isomers (Eq. 4). However, further reaction to products must proceed through the *cis*-HOCO isomer (Eq. 5), because the transition state to form H + CO_2 products from *trans*-HOCO (TS3) is predicted to be much higher than that from *cis*-HOCO (TS2). The *cis*-isomer thus plays a critical role in the OH + CO reaction, and the

[1]JILA, National Institute of Standards and Technology, and Department of Physics, University of Colorado, Boulder, CO 80309, USA. [2]Department of Chemistry, University of Florida, Gainesville, FL 32611, USA. [3]Arthur Amos Noyes Laboratory of Chemical Physics, California Institute of Technology, Pasadena, CA 91125, USA.
*Corresponding author. Email: thbu8553@jila.colorado.edu (T.Q.B.); ye@jila.colorado.edu (J.Y.)
†Present address: Honeywell International, 303 Technology Court, Broomfield, CO 80021, USA.

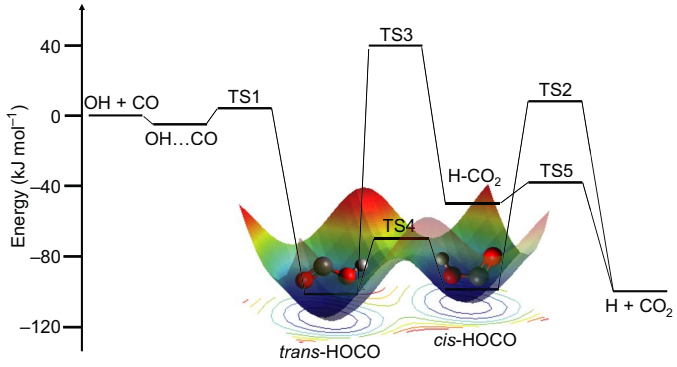

Fig. 1. The OH + CO reaction PES with energies in kilojoules per mole. The colored PES in the background depicts the HOCO isomer potential energy wells along the H–O–C–O dihedral angle (parallel to page) and O–H bond length (perpendicular to page).

isomerization dynamics determine product formation. Direct and simultaneous detection of reactant OH, intermediates *cis*-HOCO and *trans*-HOCO, and product H + CO_2 and measurement of their time dependence in the same reaction environment would reveal the coupled dynamics of all participating species from beginning to end.

Recently, Bjork *et al.* (*20*) observed the deuterated analog *trans*-DOCO formed from the OD + CO reaction under thermal conditions, providing the first direct experimental confirmation of the HOCO mechanism; however, a full understanding of the reaction mechanism requires observing the *cis*-HOCO radical and the final products. Although the *cis*-HOCO radical has been detected using molecular or ion beams (*19*, *21*, *22*) and matrix (*23*, *24*) techniques that can trap metastable species, it has not yet been observed in a thermal reaction environment as the product of OH + CO, leaving a substantial gap in our understanding of this reaction. Because experimental characterization of the OH + CO reaction kinetics is currently fragmented, the state of knowledge for the OH + CO mechanism continues to rely on theory (*3*, *6*, *8*, *18*, *25*).

We now report a direct observation and measurement of the deuterated analog *cis*-DOCO intermediate from the OD + CO reaction via time-resolved frequency comb spectroscopy, a technique for obtaining high-resolution, transient absorption spectra over a wide spectral range in the mid-infrared (IR) (λ = 3 to 5 μm) with microsecond time resolution (*20*, *26*–*28*). Using a room temperature flow cell, the OD + CO reaction is initiated at t = 0 by photodissociation of O_3 in the presence of D_2, CO, and N_2 (total pressure range, 20 to 100 torr). From real-time measurements of the time-dependent populations of reactant OD, intermediates *trans*-DOCO and *cis*-DOCO, and product CO_2 via their IR absorption spectral windows shown in Fig. 2, we disentangle the entire kinetic process by following this reaction step by step. We now have direct access to the reaction rate coefficients and branching yields of all chemically accessible product channels; to date, this provides the most comprehensive experimental observations of this multistep reaction.

RESULTS AND DISCUSSION

Figure 2A shows the gas-phase spectrum of *cis*-DOCO in the OD stretch fundamental band, which has not been observed before this work. To confirm the identification of *cis*-DOCO, we performed additional experiments to obtain an isotopic substitution spectrum. The predominately *b*-type nature of the *cis*-DOCO OD stretch band gives rise

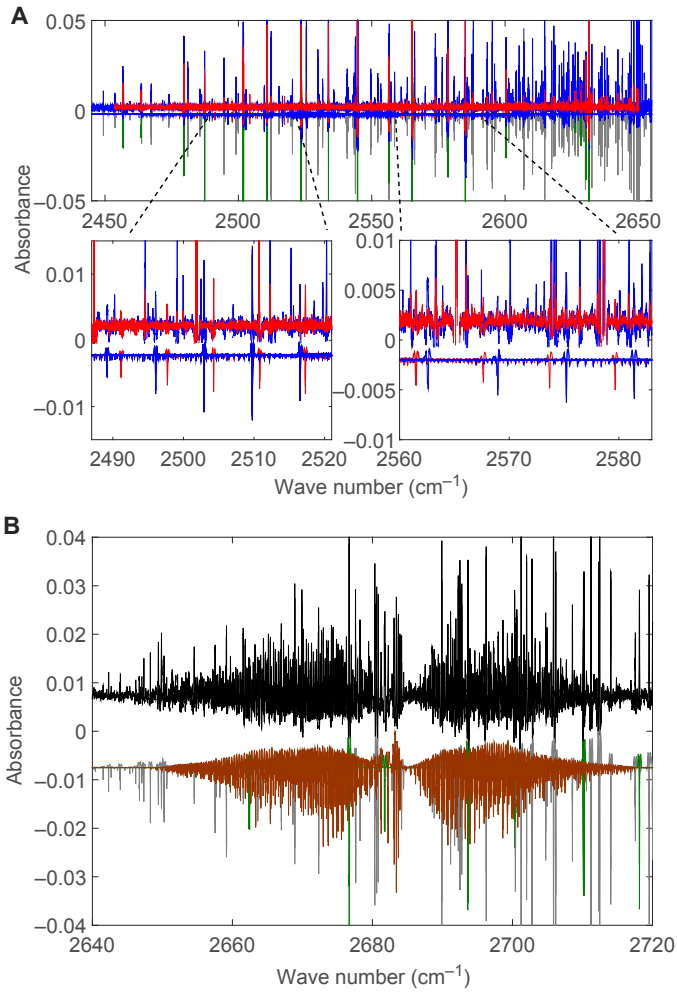

Fig. 2. Spectroscopy of DOCO isomers. (**A**) Full *cis*-DOCO spectrum (top). The data and simulation are given by positive and negative absorbances, respectively. The color codes are as follows: blue, *cis*-DO^{12}CO; red, *cis*-DO^{13}CO; green, OD; gray, D_2O. For clarity, only the simulated *cis*-DO^{12}CO and *cis*-DO^{13}CO are shown for comparison with experimental results in the zoomed-in bottom panels, where the strongest Q branches are located. (**B**) *Trans*-DOCO spectrum (black). Simulated *trans*-DOCO (brown), OD (green), and D_2O (gray) are shown as inverted absorbances. The detection spectral regions are 2400 to 2850 cm^{-1} (OD), 2450 to 2650 cm^{-1} (*cis*-DOCO) (A), 2640 to 2720 cm^{-1} (*trans*-DOCO) (B), and 2380 to 2445 cm^{-1} (CO_2). Data in (A) and (B) were obtained by integrating from t = 0 to 200 μs at a 100-μs camera integration time.

to an observed progression of Q branches, each consisting of many unresolved individual rovibrational transitions, spaced approximately 7 cm^{-1} apart (table S1). By fitting the frequencies of these spectral features, the v = 1 band origin and A rotational constant for both ^{12}C and ^{13}C isotopologues of *cis*-DOCO are obtained. The predicted and measured spectroscopic constants for both ^{12}C and ^{13}C isotopologues of *cis*-DOCO are compiled in table S2. The measured isotopic shifts to these molecular constants are then compared to their respective ab initio values predicted using second-order vibrational perturbation theory (VPT2) at the CCSD(T)/ANO1 level (table S3). The agreement between the experimental and theoretical values provides conclusive evidence for the identification of *cis*-DOCO.

The time-dependent concentrations of OD, *cis*-DOCO, *trans*-DOCO (Fig. 2B), and CO_2 are determined from the IR absorption signals; time traces at a single reaction condition are plotted in Fig. 3A. Although the

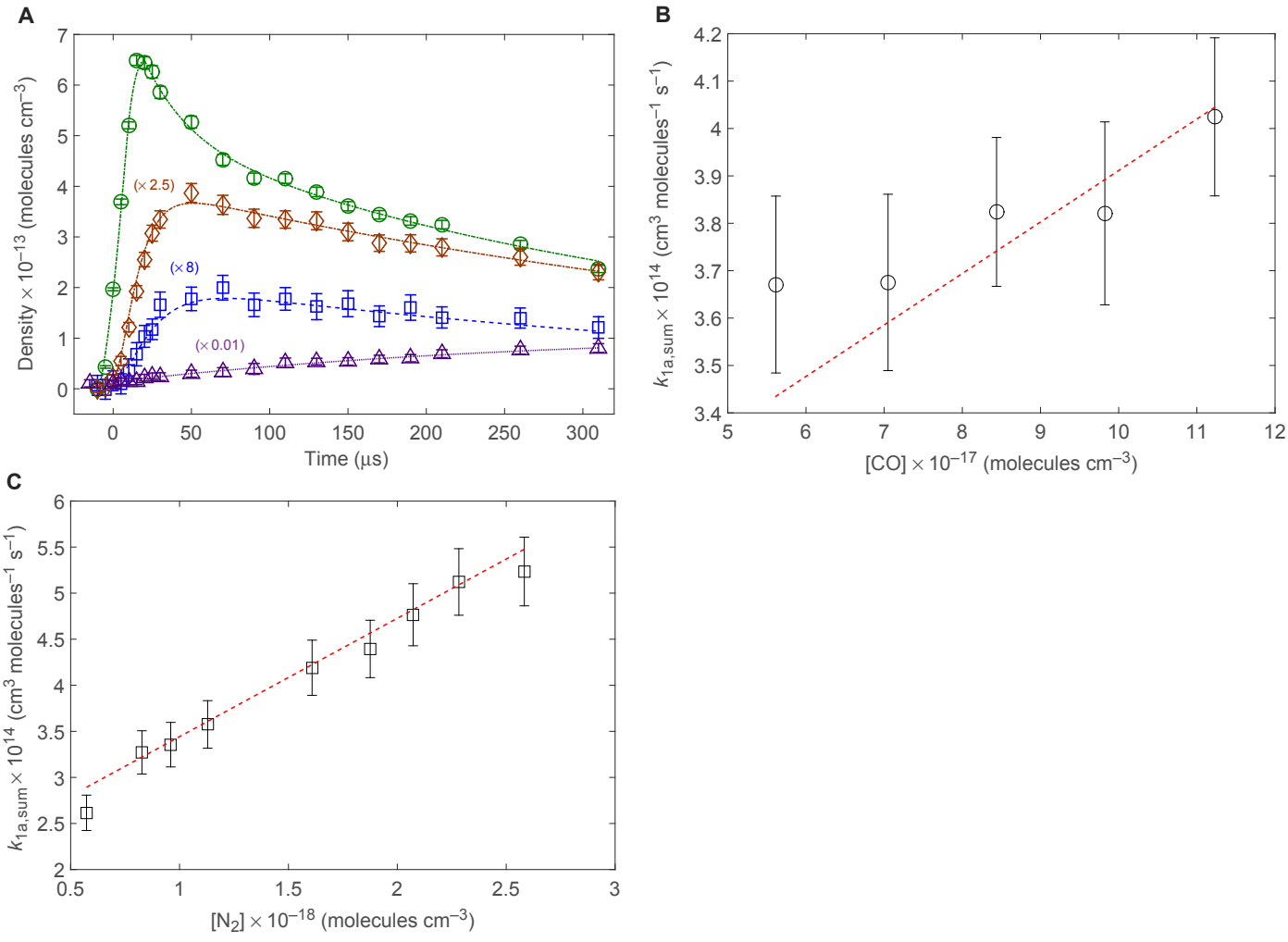

Fig. 3. Time traces of reaction components and the formation rates for the sum of DOCO isomers. (**A**) Time dependence of reactant OD (green circles), intermediates *cis*-DO^{12}CO (blue squares) and *trans*-DOCO (brown diamonds), and product CO_2 (purple triangles) obtained from fitting full experimental spectra for a sequence of time windows after the initiation of the reaction. Quantities in parenthesis are multiplicative factors used to scale the traces to fit on a single plot. The camera integration time is 20 μs for OD, *cis*-DOCO, and *trans*-DOCO and 50 μs for CO_2. Each time point corresponds to ≈400 averaged spectra. The error bars are from uncertainties in the fit and the measured densities of the gases. The dashed and dotted lines are fits of eq. S4 for OD, Eq. 6 for *trans*- and *cis*-DOCO, and eq. S8 for CO_2 using values measured from this work. (**B**) $k_{1a,sum}$ is plotted as a function of CO, whereas $[N_2]$ is held constant at 8.9×10^{17} molecules cm^{-3}. (**C**) $k_{1a,sum}$ is plotted as a function of N_2, whereas [CO] is held constant at 5.6×10^{17} molecules cm^{-3}. In both plots, $[D_2]$ and $[O_3]$ are fixed at 1.4×10^{17} and 2×10^{15} molecules cm^{-3}, respectively. The red dashed lines show the fits obtained from a multidimensional linear regression procedure described in the main text. Data in (B) and (C) were obtained at a 50-μs camera integration time. The error bars in (B) and (C) represent uncertainties from fits to Eqs. 8 and 9 and the measured densities of the gases.

reaction system is characterized by a complex set of primary and secondary reactions, as described in our earlier works (*20*, *28*), we find that at early times (t < 200 μs), we can effectively model the time dependence including only formation, isomerization, and loss processes of DOCO isomers, represented by rate coefficients $k_{1a,i}([M],T)$, $k_{iso,ij}([M],T)$, and $k_{loss,i}$ (i,j = *cis* or *trans*), respectively, with the following rate equations (Eq. 6)

$$\frac{d[cis]}{dt} = k_{1a,cis}[CO][OD]_t - k_{loss,cis}[X][cis]_t - k_{iso,ct}[cis]_t + k_{iso,tc}[trans]_t$$
$$\frac{d[trans]}{dt} = k_{1a,trans}[CO][OD]_t - k_{loss,trans}[X][trans]_t + k_{iso,ct}[cis]_t - k_{iso,tc}[trans]_t \quad (6)$$

The subscript t denotes time. The time-dependent $[cis\text{-DOCO}]_t$ and $[trans\text{-DOCO}]_t$ are denoted by $[cis]_t$ and $[trans]_t$, respectively. $k_{iso,ct}([M],T)$ and $k_{iso,tc}([M],T)$ are the pressure-dependent effective isomerization rate coefficients for *cis* → *trans* and *trans* → *cis*, respectively. k_{loss} describes the decay of DOCO from a reaction with one or more species X, and $[OD]_t$ is the time-dependent concentration of OD in the ground vibrational state. We have previously characterized vibrationally excited OD populations and lifetimes at our experimental conditions; nonequilibrium effects introduce no more than a 10% error in our current measurements (*20*). We assume that the dissociation/tunneling of thermalized *cis*-DOCO to D + CO_2, which proceeds over a high barrier (TS2), cannot compete with the other channels at these time scales.

Considering the possibility of substantial isomerization rates that may compete with the formation rate, we set out to perform experiments

to disentangle their relative effects by varying the buffer gas species and its pressure. We sought to distinguish formation from isomerization by first determining the effective bimolecular formation and loss rate coefficients for the sum of DOCO isomers, $k_{1a,sum}([M],T) \equiv k_{1a,cis}([M],T) + k_{1a,trans}([M],T)$, and a similar expression for $k_{loss,sum}$ (Eq. 7)

$$\frac{d[DOCO_{sum}]}{dt} = k_{1a,sum}[CO][OD]_t - k_{loss,sum}[X][DOCO_{sum}]_t \quad (7)$$

where $[DOCO_{sum}] \equiv [trans] + [cis]$. Using the total DOCO concentration eliminates the need to model isomerization in Eq. 6 (derived in section S2). In the low-pressure limit studied here, the DOCO formation rate obeys a termolecular rate law, in which M represents the buffer gas species (a third-body collider). In this reaction, M comprises all the high-density species present (N_2, CO, D_2, and O_3).

The solution to Eq. 7 is a convolution of the DOCO loss term with $[OD]_t$, given by the integral in Eq. 8 (u is a dummy variable). [CO] is in large excess and remains effectively constant throughout the reaction

$$[DOCO_{sum}]_t = k_{1a,sum}[CO]\int_0^t e^{-(k_{loss,sum}[X])(t-u)}[OD](u)du \quad (8)$$

The effective bimolecular rate coefficient $k_{1a,sum}([M],T)$ can be decomposed into three terms dependent on N_2, CO, and D_2 concentrations

$$k_{1a,sum} = k_{1a,sum}^{(CO)}[CO] + k_{1a,sum}^{(N2)}[N_2] + k_{1a,sum}^{(D2)}[D_2] + k_{1a,sum}^{(0)} \quad (9)$$

where $k_{1a,sum}^{(CO)}$, $k_{1a,sum}^{(N2)}$, and $k_{1a,sum}^{(D2)}$ are the termolecular rate coefficient dependence on M = CO, N_2, and D_2, respectively. $k_{1a,sum}^{(0)}$ is an offset term that accounts for additional background species. O_3 is not included in Eq. 9 because its concentration is smaller by a factor greater than 10^2 compared to the other buffer gas species. Its main contribution is to DOCO loss.

By simultaneously fitting $[DOCO_{sum}]_t$ and $[OD]_t$ from data in Fig. 3A across varying [CO], $[N_2]$, and $[D_2]$, the effective bimolecular rate coefficients for the $DOCO_{sum}$ formation, $k_{1a,sum}$, are obtained as follows. $[OD]_t$ are fit using empirically derived analytical functions (eq. S4). This spline interpolation procedure provides an analytical expression for $[OD]_t$ without making any assumptions about its formation or decay mechanisms. The observed $[DOCO_{sum}]_t$ is then fit to Eq. 8, integrating the fitted $[OD]_t$ function over the time window of −25 μs (convoluted with the finite response time of the camera) to 200 μs. The fitted parameters in Eq. 8 are $k_{1a,sum}$ and $r_{loss,sum}$; the latter is an effective first-order rate for the loss of $DOCO_{sum}$.

DOCO must be lost by reaction with one or more species, which we define as X; then, $r_{loss,sum} = k_{loss,sum}[X]$, where $k_{loss,sum}$ is a bimolecular rate coefficient. We hypothesized that $X = O_3$, because O_3 is the highest concentration candidate that is reactive with DOCO. To test this, $r_{loss,sum}$ is determined independently by measuring $[cis]_t$ and $[trans]_t$ while varying the density of O_3; the results are shown in fig. S1. The observed loss rate is proportional to O_3 and is invariant to [CO], $[N_2]$, and $[D_2]$, leading to an empirical bimolecular rate coefficient for DOCO loss to O_3, $k_{loss,sum} = 2.5(6) \times 10^{-11}$ cm^3 $molecules^{-1}$ s^{-1}, from a global fit across all CO, N_2, and D_2 data sets. We conclude that X is predominantly O_3. One possible outcome from the reaction of DOCO with O_3 is to recycle OD, which, together with the reaction of D + O_3 → OD + D, would lead to the quasi–steady state observed in $[OD]_t$ at long delay times (Fig. 3A). The direct measurement of $[OD]_t$ eliminates the need to explicitly treat the recycling in our analysis. Finally, because there is some O_2 present in the O_3 flow, some of the loss is due to reaction with O_2, which will also appear to vary linearly with O_3. Any contribution to $r_{loss,sum}$ from the reaction with O_2 is likely to be minor, because $[O_2] << [O_3]$, and in addition, the rate coefficient for DOCO + O_2 is an order of magnitude lower than that for $k_{loss,sum}$.

After establishing that $r_{loss,sum}$ is due to reaction with O_3, we next determine the effective bimolecular rate coefficients, $k_{1a,sum}$, to form DOCO from Eq. 8 for each buffer gas ([CO], $[N_2]$, and $[D_2]$). The results from experiments varying each gas concentration independently while fixing $[O_3] = 2 \times 10^{15}$ molecules cm^{-3} ($r_{loss,sum} = 5 \times 10^4$ s^{-1}) are displayed as data points in Fig. 3 (B and C) and fig. S2, respectively.

Fits of $k_{1a,sum}$ reveal that, under our conditions, CO and N_2 contribute to DOCO stabilization; there is no observable dependence on D_2 over the limited pressure range studied. To account for all three species present in each experiment, we perform a multidimensional linear regression of the data in Fig. 3 (B and C) and fig. S2 (fitted bimolecular rate coefficients) to Eq. 9 to determine the termolecular rate coefficients $k_{1a,sum}^{(CO)}$, $k_{1a,sum}^{(N2)}$, and $k_{1a,sum}^{(D2)}$, respectively. The linear fits are given as red dashed lines. In the varying CO experiment (Fig. 3B), a clear linear dependence is observed, indicating a termolecular dependence of $k_{1a,sum}$ on CO or $k_{1a,sum}^{(CO)}$. The offset in the linear fit comes from the N_2 termolecular dependence of $k_{1a,sum}$ or $k_{1a,sum}^{(N2)}$. A similar linear dependence is seen for varying N_2 (Fig. 3C), with the offset being the $k_{1a}^{(CO)}$ component. The results obtained from the multidimensional linear regression are $k_{1a,sum}^{(CO)} = 8.5^{4.5}_{-5.4} \times 10^{-33}$ cm^6 $molecules^{-2}$ s^{-1}, $k_{1a,sum}^{(N2)} = 1.3^{0.4}_{-0.5} \times 10^{-32}$ cm^6 $molecules^{-2}$ s^{-1}, and $k_{1a,sum}^{(D2)} = 9.6^{23}_{-24} \times 10^{-33}$ cm^6 $molecules^{-2}$ s^{-1}. We observe an additional offset in the effective bimolecular rate constant, $k_{1a,sum}^{(0)} = 1.5^{0.7}_{-0.8} \times 10^{-14}$ cm^3 $molecules^{-1}$ s^{-1}. More than 80% of the offset term, $k_{1a,sum}^{(0)}$, can be accounted for by a combination of the upper bound of $k_{1a,sum}^{(D2)}$ and competition from DOCO loss processes ($r_{loss,sum}$). The D_2 concentrations are too low (<10% of total gas) to determine $k_{1a,sum}^{(D2)}$ accurately. Discussions of all statistical and systematic error sources for $k_{1a,sum}$ are found in table S4.

Up to this point, we have considered only the formation kinetics of the two DOCO isomers together and thus could neglect *cis*/*trans* isomerization. To resolve the dynamical coupling of the isomer-specific formation and isomerization kinetics, we measure the time dependence of the [*trans*]/[*cis*] ratio at nine different partial pressures of CO. Figure 4A shows five representative experimental time traces of this ratio, which are offset vertically for reasons of clarity. The observed time evolution of the [*trans*]/[*cis*] ratio to a steady-state value for each trace indicates a transition between two distinct time regimes: the early-time DOCO formation (k_{1a}) and subsequent relaxation by *trans*/*cis* isomerization (k_{iso}).

We hypothesize that the observed time dependence of the [*trans*]/[*cis*] ratios can be described by a simple kinetic model given by eqs. S9 to S17 and qualitatively understood as follows. The nascent [*trans*]/[*cis*] ratio extrapolated to $t \approx 0$ μs (before any thermal, canonical isomerization) is determined only by the ratio of the formation rate coefficients for the two isomers ($k_{1a,trans}/k_{1a,cis}$). This initial ratio then rises/decays to a steady-state value. The rate of the exponential rise/decay increases with the sum of $k_{iso,tc}$ and $k_{iso,ct}$ and is an indication of how fast the *trans* to *cis* populations approach this steady state. During this time ($t < 50$ μs), formation and isomerization compete. At $t > 50$ μs, the isomerization reaction dominates and establishes steady-state populations of *trans* and *cis* isomers that persist at long times. If the formation and loss processes for DOCO are slow relative to isomerization, the *trans* and *cis* isomers are in

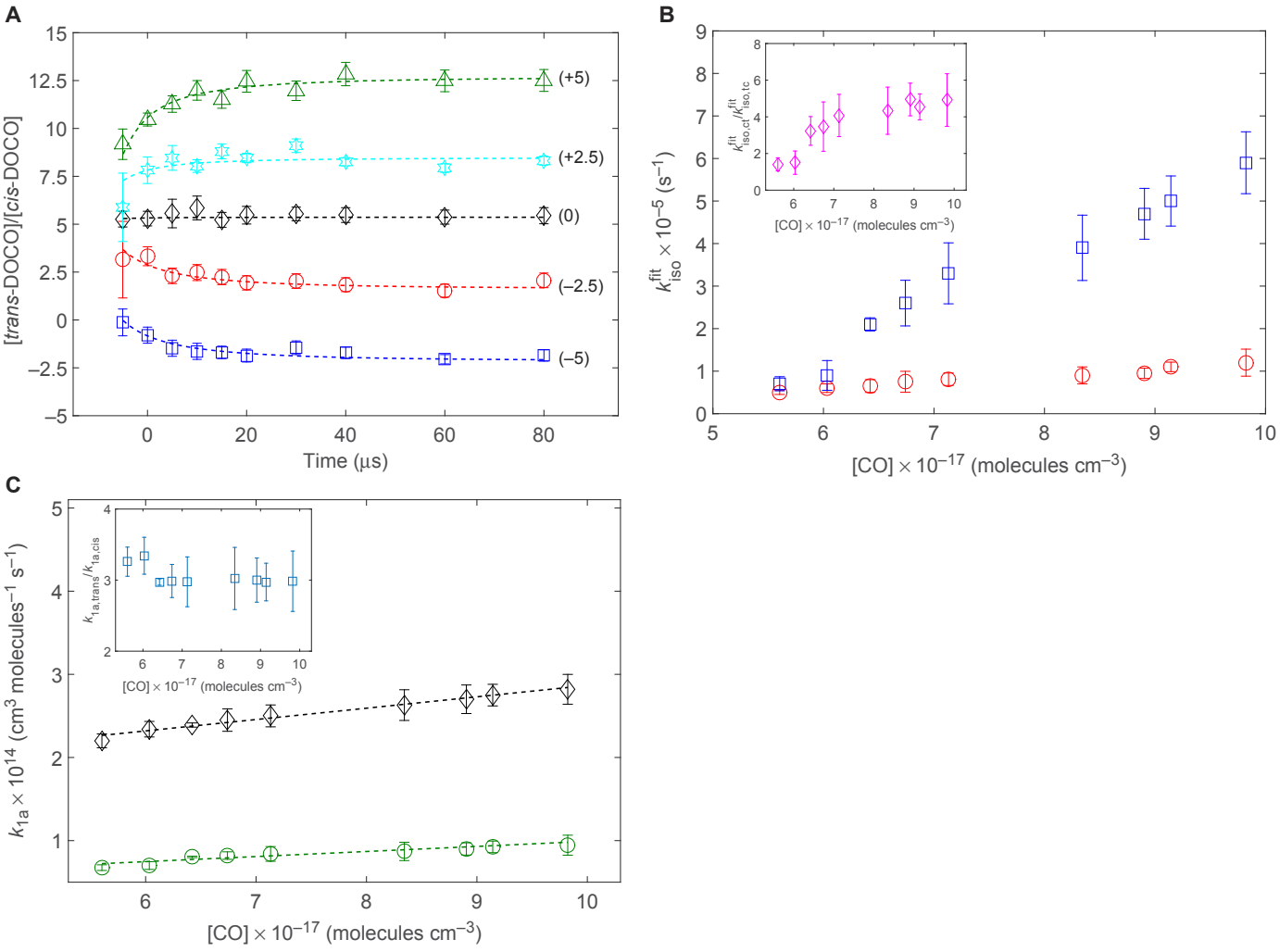

Fig. 4. DOCO formation and isomerization kinetics. (**A**) Ratio of [*trans*-DOCO] to [*cis*-DOCO] as a function of time for different CO concentrations. The CO concentrations are 5.6×10^{17}, 6.0×10^{17}, 6.4×10^{17}, 6.7×10^{17}, and 7.1×10^{17} molecules cm^{-3} for blue squares, red circles, black diamonds, cyan hexagons, and green triangles, respectively. For these experiments, [N_2], [D_2], and [O_3] were fixed to 8.9×10^{17}, 1.4×10^{17}, and 2×10^{15} molecules cm^{-3}, respectively. The arbitrary *y*-axis offsets of −5, −2.5, 0, +2.5, and +5, respectively, are added for ease of viewing. At high [CO] (>6.4×10^{17} molecules cm^{-3}), all curves reach the same asymptotic value within experimental uncertainties. The dashed lines are fits of the rate equation model to the data. Data were obtained at a 20-μs camera integration time. The error bars represent uncertainties from the spectral fit and measured densities of gases. (**B**) Fitted isomerization rate coefficients for *cis* → *trans* ($k_{iso,ct}^{fit}$; blue squares) and *trans* → *cis* ($k_{iso,tc}^{fit}$; red circles). The ratio of $k_{iso,ct}^{fit}/k_{iso,tc}^{fit}$ as a function of [CO] is given in the inset. (**C**) Fitted effective bimolecular formation rate coefficients (k_{1a}) for *trans*-DOCO ($k_{1a,trans}$; black diamonds) and *cis*-DOCO ($k_{1a,cis}$; green squares). The ratio of the formation rate coefficients $k_{1a,trans}/k_{1a,cis}$ as a function of [CO] is given in the inset. The error bars in (B) and (C) represent uncertainties from the individual parameter variance and covariance between $k_{1a,sum}$ and k_{iso}.

equilibrium. The [*trans*]/[*cis*] ratio then becomes independent of [CO] and [*trans*]/[*cis*] = $k_{iso,ct}/k_{iso,tc} = K_{iso}$, the equilibrium constant (K_{iso}) for DOCO isomerization.

To quantify the isomerization and isomer-specific formation rate coefficients, we fit time-dependent [*trans*]/[*cis*] ratios by extending Eq. 6 to include the rate equation for OD formation and decay (eq. S7). The dashed lines ($\chi^2_{red} \approx 0.9$ to 1.7) in Fig. 4A are results obtained from fitting the formation rate coefficients, $k_{1a,cis}$ and $k_{1a,trans}$, and isomerization coefficients, $k_{iso,tc}$ and $k_{iso,ct}$, to all nine experimental data sets (differing in CO pressures) simultaneously. Here, $k_{1a,sum} = k_{1a,cis} + k_{1a,trans}$ is fixed to the value measured previously for the sum of isomers (in Fig. 3B). We also assume that the loss rate is isomer-independent and fix k_{loss} to the fitted value in Eq. 8.

The CO dependence of the fitted isomer-specific k_{iso}^{fit} and k_{1a} is given in Fig. 4, B and C, respectively, and compiled in table S5. Both the formation and thermalized isomerization rate constants are observed to be linear with pressure and hence in the low-pressure limit. For the termolecular formation rate coefficients, we find that $k_{1a,trans}^{(CO)} = 1.4(4) \times 10^{-32}$ cm^6 molecules^{-2} s^{-1} and $k_{1a,cis}^{(CO)} = 6(2) \times 10^{-33}$ cm^6 molecules^{-2} s^{-1} from fitting the data in Fig. 4C. The ratio of the fitted isomerization rate coefficients (Fig. 4B, inset), however, varies with CO concentration and only becomes constant at higher [CO]. This ratio should be a constant and independent of [CO]; this variation, which reflects different values of the steady-state [*trans*]/[*cis*] ratio, indicates the existence of competition between DOCO isomerization, bimolecular formation, and reactive loss. The fitted isomerization rates

are thus empirical, and we designate them as apparent isomerization rate coefficients $k_{iso,tc}^{fit}$ and $k_{iso,ct}^{fit}$.

Figure 4A shows that with increasing [CO], the transition from decay to rise behavior in the [*trans*]/[*cis*] ratio occurs at approximately [CO] = 6.5×10^{17} molecules cm^{-3}. This trend can now be explained by comparing the $k_{iso,ct}^{fit}/k_{iso,tc}^{fit}$ and $k_{1a,trans}/k_{1a,cis}$ ratios given in the insets of Fig. 4, B and C, respectively. This transition is also the intersection point of the decreasing $k_{iso,ct}^{fit}/k_{iso,tc}^{fit}$ and increasing $k_{1a,trans}/k_{1a,cis}$. At the lowest CO pressures, the formation, isomerization, and loss rates all have similar magnitudes ($\approx 10^4$ s^{-1}), and therefore, these processes compete.

Additional evidence for this interplay can be found in the observed ratio of $k_{iso,ct}^{fit}/k_{iso,tc}^{fit}$ from the inset of Fig. 4B. Under these conditions, the fitted ratio of $k_{iso,ct}^{fit}/k_{iso,tc}^{fit}$ varies apparently with CO pressure, indicating that these empirical parameters in our model include isomer-specific formation and loss processes. However, at higher pressures ([CO] > 6.4×10^{17} molecules cm^{-3}), isomerization dominates ($\approx 10^5$ s^{-1}) and $k_{iso,ct}^{fit}/k_{iso,tc}^{fit}$ converges to a constant value, which suggests that the high pressure ratio is the true ratio of isomerization rates and hence the pressure-independent equilibrium constant, $K_{iso} \approx 5(2):1$.

The *trans*- and *cis*-DOCO equilibrium constant is a fundamental thermodynamic quantity. Our measured equilibrium constant is consistent with that determined from the experimental well depths of HOCO isomers reported by Johnson and co-workers (*19*). We can also compare our measurement with predictions by state-of-the-art calculations. Using a theoretical method that combines semiclassical transition state theory (SCTST) (*29*–*31*) with two-dimensional (2D) master equations (*18*, *25*, *32*), the calculated pressure-dependent isomerization rate coefficients are displayed in fig. S3. The theoretical equilibrium constant is $K_{iso,th} \approx 14:1$. Although the measured value disagrees with theory, a change of ≈2 kJ mol^{-1} in the relative energies (enthalpy) of *cis*- and *trans*-DOCO would account for the difference in the measured and predicted equilibrium constants. Because the entropy component of the K_{eq} calculation comes from the use of theoretical rovibrational parameters that are in good agreement with the experimentally measured values, it is unlikely that entropy accounts for a majority of the discrepancy. Our observed equilibrium concentrations also rely on ab initio calculations of the absorption cross sections of *cis*- and *trans*-DOCO, which are challenging for accurate determination.

New experimental insight into the energy transfer processes is obtained from the formation rate dependence on collision partner and total pressure for both *cis*- and *trans*-DOCO isomers. We demonstrate that DOCO exhibits isomer-specific formation rates. CO is more than twice as effective in collisionally stabilizing *trans*-DOCO* compared to *cis*-DOCO*. The unusually large enhancement by the CO collision partner for the *trans*-DOCO isomer relative to *cis*-DOCO may be a consequence of complex formation between *trans*-DOCO* and CO from a stronger interaction potential, which would facilitate energy transfer. This mechanism is further supported by spectroscopic observation of the *trans*-HOCO(CO) complex in the molecular beam environment by Oyama *et al.* (*33*).

Finally, the identification and quantification of *cis*-DOCO, *trans*-DOCO, and D + CO_2 account for all possible branching pathways for OD + CO. It is now experimentally possible to deconstruct the effective bimolecular rate coefficient k_1 in the low-pressure limit as a sum of elementary reaction steps, that is, $k_1([M],T) = k_{1a,cis}([M],T) + k_{1a,trans}([M],T) + k_{1b}(T)$, where $k_{1b}(T)$ is the bimolecular rate coefficient for the pressure-independent well skipping the D + CO_2 channel (*6*, *7*, *28*). This approximation is valid in the low-pressure limit, provided that k_1 is only strongly dependent on k_{1a} while k_{1b} remains constant with total pressure and collision partner. The latter is independently verified from our measurements of the pressure-dependent formation rate of CO_2 (*28*). Previously, k_1 was determined only with contributions from *trans*-DOCO and CO_2. Mass balance dictates that *cis*-DOCO also contributes to the total k_1; the pressure dependence of k_1 has been plotted in fig. S4. The observed agreement in k_1 with previous studies by Golden *et al.* (*8*) and Paraskevopoulos and Irwin (*11*) provides additional confirmation that k_1 can be treated as a sum of the rate coefficients of independent channels, k_{1a} and k_{1b}, in the low-pressure limit. The k_{1b} value measured previously (*28*) reproduces the measured $[CO_2]_t$ in this work (Fig. 3A, dotted line fit to eq. S8), which provides additional confirmation of the OD + CO → D + CO_2 channel. We note that at t > 300 μs, $[CO_2]$ significantly exceeds [OD] because (i) there are no known reactive channels causing CO_2 loss and (ii) secondary reactions that produce CO_2 (for example, DOCO + O_3 → OD + CO_2 + O_2) result in its accumulated concentration.

CONCLUSIONS

We have unambiguously identified and quantified the time-dependent concentrations of all the reactant, intermediate, and product channels in the direct kinetics of OD + CO using time-resolved frequency comb spectroscopy. Each step of the reaction was analyzed to obtain detailed information about the elementary chemical reactions and product branching ratios. How each step quantitatively contributes to the apparent reaction rate coefficient k_1—the main observable for previous studies—is now experimentally confirmed. In addition, new insights into both the reaction mechanism and the energy transfer processes from the observed differences in the formation rate and reactivity of DOCO isomers are obtained. For the first time, these experimental observations capture DOCO dynamics, where the formation of DOCO is directly followed by isomerization reactions between the *cis*- and *trans*-DOCO isomers. Typically, isomers of intermediate species are either observed in equilibrium or isolated (*34*, *35*): To see the transition in this intermediate regime is unusual and highlights the richness of the reaction landscape. Finally, we anticipate that the next exciting frontier for the OH + CO reaction is in the low-temperature regime, where tunneling is particularly conspicuous. With the rapid emergence and success of cold molecule physics (*36*), the OH + CO reaction provides an ideal system to learn new physics and chemistry ranging from cold to the ultracold regime, especially from the perspective of quantum control of chemical reactions.

MATERIALS AND METHODS

Time-resolved frequency comb spectroscopy

The OD + CO reaction was initiated in a room temperature ($T \approx 295$ K) flow cell enclosed by high-reflectivity mirrors (for cavity-enhanced absorption spectroscopy). Absorption spectra were obtained from a mid-IR frequency comb (probe beam) propagating collinearly with the cavity axis. Details for the frequency comb source, enhancement cavity, and dispersive spectrometer can be found in previous reports (*20*, *27*). Ultraviolet light at 266 nm (≈30 mJ per pulse and ≈10 ns) orthogonal to the cavity axis photodissociated O_3 at t = 0, which produces $O(^1D)$ and O_2 at a near-unity yield. In the presence of D_2 gas, the reaction $O(^1D) + D_2$ produced OD(v = 0 to 4) and D atoms. OD(v > 0) populations were rapidly quenched to the vibrational ground state at our experimental conditions. OD($v \geq 0$) internal state distributions were thermalized at t > 10 μs (*20*). Addition of CO gas initiated the OD + CO reaction.

The total pressure range for all experiments was 20 to 100 torr. The reaction kinetics was obtained by setting a variable time delay between the photolysis pulse and the IR probe beam acquisition.

Several key experimental modifications have led to an improvement of the measurement signal-to-noise ratio compared to our previous work (*20*). The absorption sensitivity and spectral coverage were improved by the use of high-finesse mirrors with a larger bandwidth (≈3.6 to 4.2 μm). This broad spectral span granted access to a larger number of species formed from OD + CO, including OD ($v \geq 0$), DO_2, CO_2, *cis*-DOCO, and *trans*-DOCO. To observe each species, we tuned the optical parametric oscillator wavelength to its respective spectral windows. The 266-nm photolysis beam profile was shaped to be 130 mm × 6 mm to optimize the production of DOCO and spatial overlap with the mid-IR probe beam. We also used a retroreflector mirror for the photolysis beam to double the photolysis fraction. These combined changes have resulted in a net threefold increase in the measured signal of *trans*-DOCO relative to the previous apparatus.

Data extraction and analysis

Spectral fitting

The total intracavity absorbance was fit to a linear sum of absorbances for molecular species A, B, etc.

$$A(\tilde{\nu}) = -\log\left(\frac{I_S(\tilde{\nu})}{I_R(\tilde{\nu})}\right) = l_{eff}[n_A(t)\sigma_A(\tilde{\nu}) + n_B(t)\sigma_B(\tilde{\nu}) + \ldots] \quad (10)$$

where $A(\tilde{\nu})$ is the cavity absorbance, n_p (p = A, B, etc.) is the molecular density (in molecules per cubic centimeter), σ_p is the molecular absorption cross section (in square centimeters), l_{eff} is the effective absorption path length (in centimeters), and $\tilde{\nu}$ is the wave number (in reciprocal centimeters). The reference intensity, $I_R(\tilde{\nu})$, was recorded 4 ms before the photolysis pulse, and the signal intensity, $I_S(\tilde{\nu})$, was recorded after the photolysis pulse at variable delay time t.

Spectral line intensities

The OD, D_2O, and *trans*-DOCO line positions and intensities used in this work have been described previously (*20*). The CO_2 line positions and intensities were obtained from HITRAN2012 (*37*). The *cis*-DOCO spectral parameters compiled in table S2 were used to simulate the rovibrational spectrum in PGOPHER (*38*). The theoretical *cis*-DOCO $v = 1$ band strength of $S_{cis\text{-}DOCO} = 14.4124$ km mol^{-1} was calculated using VPT2 at the CCSD(T)/ANO1 level of theory.

Photolysis path length and finesse

The effective absorption path length, l_{eff}, was determined from the width of the photolysis beam, l_{phot}, and the cavity finesse, F, as

$$l_{eff} = \frac{\beta F l_{phot}}{\pi} \quad (11)$$

where $\beta = 1$. The cavity finesse as a function of wavelength was measured using the cavity ring-down technique. From Eq. 11, the effective path length was 331 ± 26 m at the peak finesse at 3920 nm. This effective absorption path length as a function of wavelength was used to determine the absolute densities displayed in Fig. 3A. However, the $k_{1a,sum}$ measurements are independent of finesse because we calculated the time derivative of [DOCO] normalized to $[OD]_t$, which cancels out the path length contribution.

SUPPLEMENTARY MATERIALS

Supplementary material for this article is available at http://advances.sciencemag.org/cgi/content/full/4/1/eaao4777/DC1

section S1. *cis*-DOCO isotope shift and spectral parameters
section S2. $k_{1a,sum}$ fitting
section S3. Theoretical calculations for OD + CO
section S4. k_1 for OD + CO as a function of N_2
table S1. Experimental spectral features for *cis*-$DO^{12}CO$ and *cis*-$DO^{13}CO$ and their rovibrational assignments.
table S2. Summary of spectral parameters for *cis*-$DO^{12}CO$ and *cis*-$DO^{13}CO$.
table S3. Comparison of experimental and theoretical isotopic shifts for *cis*-DOCO.
table S4. Summary of statistical and systematic errors for $k_{1a,sum}$.
table S5. Summary of fitted rate coefficients.
fig. S1. Variation of $r_{loss,sum}$ with O_3 concentration.
fig. S2. Variation of $k_{1a,sum}$ with D_2 concentration.
fig. S3. Calculated *cis*/*trans* isomerization rates for DOCO isomers using SCTST and 2D master equations.
fig. S4. Measured k_1 comparison with previous works.

REFERENCES AND NOTES

1. D. Herschbach, Molecular collisions, from warm to ultracold. *Faraday Discuss.* **142**, 9–23 (2009).
2. J. R. Barker, D. M. Golden, Master equation analysis of pressure-dependent atmospheric reactions. *Chem. Rev.* **103**, 4577–4592 (2003).
3. H. Guo, Quantum dynamics of complex-forming bimolecular reactions. *Int. Rev. Phys. Chem.* **31**, 1–68 (2012).
4. A. Fernández-Ramos, J. A. Miller, S. J. Klippenstein, D. G. Truhlar, Modeling the kinetics of bimolecular reactions. *Chem. Rev.* **106**, 4518–4584 (2006).
5. J. S. Francisco, J. T. Muckerman, H.-G. Yu, HOCO radical chemistry. *Acc. Chem. Res.* **43**, 1519–1526 (2010).
6. D. Fulle, H. F. Hamann, H. Hippler, J. Troe, High pressure range of addition reactions of HO. II. Temperature and pressure dependence of the reaction HO+CO⇔HOCO→H+CO_2. *J. Chem. Phys.* **105**, 983–1000 (1996).
7. C. W. Larson, P. H. Stewart, D. M. Golden, Pressure and temperature-dependence of reactions proceeding via a bound complex. An Approach for combustion and atmospheric chemistry modelers. Application to HO+CO → [HOCO] → H+CO_2. *Int. J. Chem. Kinet.* **20**, 27–40 (1988).
8. D. M. Golden, G. P. Smith, A. B. McEwen, C.-L. Yu, B. Eiteneer, M. Frenklach, G. L. Vaghjiani, A. R. Ravishankara, F. P. Tully, OH(OD)+CO: Measurements and an optimized RRKM fit. *J. Phys. Chem. A* **102**, 8598–8606 (1998).
9. D. C. McCabe, T. Gierczak, R. K. Talukdar, A. R. Ravishankara, Kinetics of the reaction OH + CO under atmospheric conditions. *Geophys. Res. Lett.* **28**, 3135–3138 (2001).
10. A. R. Ravishankara, R. L. Thompson, Kinetic study of the reaction of OH with CO from 250 to 1040 K. *Chem. Phys. Lett.* **99**, 377–381 (1983).
11. G. Paraskevopoulos, R. S. Irwin, The pressure depdendence of the rate constant of the reaction of OD radicals with CO. *Chem. Phys. Lett.* **93**, 138–143 (1982).
12. G. Paraskevopoulos, R. S. Irwin, The pressure dependence of the rate constant of the reaction of OH radicals with CO. *J. Chem. Phys.* **80**, 259–266 (1984).
13. M. J. Frost, P. Sharkey, I. W. M. Smith, Energy and structure of the transition states in the reaction OH+CO → H+CO_2. *Faraday Discuss.* **91**, 305–317 (1991).
14. M. J. Frost, P. Sharkey, I. W. M. Smith, Reaction between hydroxyl (deuteroxyl) radicals and carbon monoxide at temperatures down to 80 K: Experiment and theory. *J. Phys. Chem.* **97**, 12254–12259 (1993).
15. J. Brunning, D. W. Derbyshire, I. W. M. Smith, M. D. Williams, Kinetics of OH(v=0, 1) and OD(v = 0, 1) with CO and the mechanism of the OH + CO reaction. *J. Chem. Soc. Faraday Trans. 2* **84**, 105–119 (1988).
16. R. Forster, M. Frost, D. Fulle, H. F. Hamann, H. Hippler, A. Schlepegrell, J. Troe, High-pressure range of the addition of HO to HO, NO, NO_2, AND CO. I. Saturated laser induced fluorescence measurements at 298 K. *J. Chem. Phys.* **103**, 2949–2958 (1995).
17. A. J. Hynes, P. H. Wine, A. R. Ravishankara, Kinetics of the OH + CO reaction under atmospheric conditions. *J. Geophys. Res. Atmos.* **91**, 11815–11820 (1986).
18. T. L. Nguyen, B. C. Xue, R. E. Weston Jr., J. R. Barker, J. F. Stanton, Reaction of HO with CO: Tunneling is indeed important. *J. Phys. Chem. Lett.* **3**, 1549–1553 (2012).
19. C. J. Johnson, R. Otto, R. E. Continetti, Spectroscopy and dynamics of the HOCO radical: Insights into the OH + CO → H + CO_2 reaction. *Phys. Chem. Chem. Phys.* **16**, 19091–19105 (2014).
20. B. J. Bjork, T. Q. Bui, O. H. Heckl, P. B. Changala, B. Spaun, P. Heu, D. Follman, C. Deutsch, G. D. Cole, M. Aspelmeyer, M. Okumura, J. Ye, Direct frequency comb measurement of OD + CO → DOCO kinetics. *Science* **354**, 444–448 (2016).
21. T. Oyama, W. Funato, Y. Sumiyoshi, Y. Endo, Observation of the pure rotational spectra of *trans*- and *cis*-HOCO. *J. Chem. Phys.* **134**, 174303 (2011).

22. M. C. McCarthy, O. Martinez Jr., B. A. McGuire, K. N. Crabtree, M.-A. Martin-Drumel, J. F. Stanton, Isotopic studies of *trans*- and *cis*-HOCO using rotational spectroscopy: Formation, chemical bonding, and molecular structures. *J. Chem. Phys.* **144**, 124304 (2016).
23. D. E. Milligan, M. E. Jacox, Infrared spectrum and structure of intermediates in the reaction of OH with CO. *J. Chem. Phys.* **54**, 927–942 (1971).
24. Z. Mielke, A. Olbert-Majkut, K. G. Tokhadze, Photolysis of the OC···HONO complex in low temperature matrices: Infrared detection and ab initio calculations of nitrosoformic acid, HOC(O)NO. *J. Chem. Phys.* **118**, 1364–1377 (2003).
25. R. E. Weston Jr., T. L. Nguyen, J. F. Stanton, J. R. Barker, HO + CO reaction rates and H/D kinetic isotope effects: Master equation models with ab initio SCTST rate constants. *J. Phys. Chem. A* **117**, 821–835 (2013).
26. M. J. Thorpe, K. D. Moll, R. J. Jones, B. Safdi, J. Ye, Broadband cavity ringdown spectroscopy for sensitive and rapid molecular detection. *Science* **311**, 1595–1599 (2006).
27. A. J. Fleisher, B. J. Bjork, T. Q. Bui, K. C. Cossel, M. Okumura, J. Ye, Mid-infrared time-resolved frequency comb spectroscopy of transient free radicals. *J. Phys. Chem. Lett.* **5**, 2241–2246 (2014).
28. T. Q. Bui, B. J. Bjork, P. B. Changala, O. H. Heckl, B. Spaun, J. Ye, OD + CO → D + CO_2 branching kinetics probed with time-resolved frequency comb spectroscopy. *Chem. Phys. Lett.* **683**, 91–95 (2017).
29. B. Widom, Molecular transitions and chemical reaction rates: Stochastic model relates the rate of a chemical reaction to the underlying transition probabilities. *Science* **148**, 1555–1560 (1965).
30. W. H. Miller, Semiclassical theory for non-separable systems: Construction of "good" action-angle variables for reaction-rate constants. *Faraday Discuss. Chem. Soc.* **62**, 40–46 (1977).
31. R. Hernandez, W. H. Miller, Semiclassical transition state theory. A new perspective. *Chem. Phys. Lett.* **214**, 129–136 (1993).
32. N. J. B. Green, P. J. Marchant, M. J. Perona, M. J. Pilling, S. H. Robertson, Forward and reverse rate coefficients in equilibrating isomerization reactions. *J. Chem. Phys.* **96**, 5896–5907 (1992).
33. T. Oyama, Y. Sumiyoshi, Y. Endo, Pure rotational spectra of the CO-*trans*-HOCO complex. *J. Chem. Phys.* **137**, 154307 (2012).
34. J. L. Fry, S. A. Nizkorodov, M. Okumura, C. M. Roehl, J. S. Francisco, P. O. Wennberg, *Cis-cis* and *trans-perp* HOONO: Action spectroscopy and isomerization kinetics. *J. Chem. Phys.* **121**, 1432–1448 (2004).
35. A. K. Mollner, S. Valluvadasan, L. Feng, M. K. Sprague, M. Okumura, D. B. Milligan, W. J. Bloss, S. P. Sander, P. T. Martien, R. A. Harley, A. B. McCoy, W. P. L. Carter, Rate of gas phase association of hydroxyl radical and nitrogen dioxide. *Science* **330**, 646–649 (2010).
36. J. L. Bohn, A. M. Rey, J. Ye, Cold molecules: Progress in quantum engineering of chemistry and quantum matter. *Science* **357**, 1002–1010 (2017).
37. L. S. Rothman, I. E. Gordon, Y. Babikov, A. Barbe, D. C. Benner, P. F. Bernath, M. Birk, L. Bizzocchi, V. Boudon, L. R. Brown, A. Campargue, K. Chance, E. A. Cohen, L. H. Coudert, V. M. Devi, B. J. Drouin, A. Fayt, J.-M. Flaud, R. R. Gamache, J. J. Harrison, J.-M. Hartmann, C. Hill, J. T. Hodges, D. Jacquemart, A. Jolly, J. Lamouroux, R. J. Le Roy, G. Li, D. A. Long, O. M. Lyulin, C. J. Mackie, S. T. Massie, S. Mikhailenko, H. S. P. Müller, O. V. Naumenko, A. V. Nikitin, J. Orphal, V. Perevalov, A. Perrin, E. R. Polovtseva, C. Richard, M. A. H. Smith, E. Starikova, K. Sung, S. Tashkun, J. Tennyson, G. C. Toon, Vl. G. Tyuterev, G. Wagner, The HITRAN2012 molecular spectroscopic database. *J. Quant. Spectrosc. Radiat. Transf.* **130**, 4–50 (2013).
38. C. M. Western, PGOPHER: A program for simulating rotational, vibrational and electronic spectra. *J. Quant. Spectrosc. Radiat. Transf.* **186**, 221–242 (2017).

Acknowledgments: We thank J. M. Bowman and H. Guo for stimulating discussions. **Funding:** We acknowledge the financial support from the Air Force Office of Scientific Research (FA9550-15-1-0111 P00002), Defense Advanced Research Projects Agency Spectral Combs from UV to THz, National Institute of Standards and Technology, and NSF JILA Physics Frontier Center (NSF PHY-1734006). J.F.S. and T.L.N. acknowledge the financial support from the U.S. Department of Energy, Office of Basic Energy Sciences, under award number DE-FG02-07ER15884. M.O. acknowledges the support of the NSF (grant CHE-1413712) and NASA's Upper Atmosphere Research Program. T.Q.B. is supported by the National Research Council Research Associate Fellowship, and P.B.C. is supported by the NSF Graduate Research Fellowships Program. **Author contributions:** T.Q.B., B.J.B., M.O., and J.Y. conceived and designed the experiments. T.Q.B., B.J.B., P.B.C., and J.Y. discussed and implemented the experimental technique. T.Q.B. and B.J.B. analyzed all the data. T.L.N. and J.F.S. provided the supporting theory. All authors contributed to technical discussions and writing of the manuscript. **Competing interests:** All authors declare that they have no competing interests. **Data and materials availability:** Data are archived on a network-attached storage drive located at JILA. All data needed to evaluate the conclusions in the paper are present in the paper and/or the Supplementary Materials. Additional data related to this paper may be requested from the authors.

Submitted 25 July 2017
Accepted 7 December 2017
Published 12 January 2018
10.1126/sciadv.aao4777

Citation: T. Q. Bui, B. J. Bjork, P. B. Changala, T. L. Nguyen, J. F. Stanton, M. Okumura, J. Ye, Direct measurements of DOCO isomers in the kinetics of OD + CO. *Sci. Adv.* **4**, eaao4777 (2018).

Direct measurements of DOCO isomers in the kinetics of OD + CO

Thinh Q. Bui, Bryce J. Bjork, P. Bryan Changala, Thanh L. Nguyen, John F. Stanton, Mitchio Okumura and Jun Ye

Sci Adv **4** (1), eaao4777.
DOI: 10.1126/sciadv.aao4777